NANO LETTERS

pubs.acs.org/NanoLett
Letter

Self-Aligned Multilayered Nitrogen Vacancy Diamond Nanoparticles for High Spatial Resolution Magnetometry of Microelectronic Currents

Yash Gokhale,[▽] Brandon S. Coventry,[▽] Tsani Rogers, Maya Lines, Anna Vena, Jack Phillips, Tianxiang Zhu, Ilhan Bok, Dariana Troche, Mitchell Glodowski, Adam Vareberg, Suyash Bhatt, Alireza Ousati Ashtiani, Kevin W. Eliceiri, and Aviad Hai*

Cite This: https://doi.org/10.1021/acs.nanolett.5c00656

ABSTRACT: Nitrogen vacancy diamond nanoparticles (NVNPs) are increasingly integrated with methods for optical detection of magnetic resonance (ODMR), providing new opportunities spanning the visualization of magnetic fields in microelectronic circuits, environmental sensing, and biology. However, only a small number of studies utilize aggregates of NVNPs for surface-wide magnetometry, with the fact that spin orientations in aggregate NVNPs are inherently misaligned, precluding proper magnetic field detection, compared with expensive monocrystalline diamonds. A post-processing method for layering NVNPs with aligned center orientations can potentially facilitate superior NV magnetometry by allowing sensitive detection with a simplified probe preparation. We present novel technology for creating densely stacked NVNP monolayers with inherent interlayer alignment for sensitive measurement of local field perturbations in microelectronic traces. We establish spatial characteristics of deposited aggregates and demonstrate their ability to capture dipoles from conducting microwires via ODMR. Our approach forms a novel accessible protocol that can be used for broad applications in micromagnetometry.

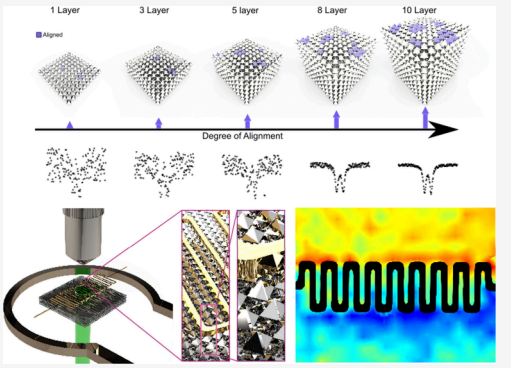

KEYWORDS: *Nitrogen Vacancy (NV), Nanodiamonds, Nanoparticles, Self-assembly, ODMR, microelectronics*

Nitrogen vacancy (NV) diamond magnetometry harnesses optomagnetic sensitivities of an electron pair near vacancy centers of irradiated diamond substrates to measure femtotesla (fT) level magnetic fields at nanometer-scale resolution.[1−5] By relying on optically detected magnetic resonance (ODMR) of electron spectra splitting in proportion to nearby magnetic fields,[6−8,5,9] a multitude of applications have been realized in quantum computing,[10−14] characterization of magnetic nanostructures,[15−18] and investigation of biological and neural magnetism.[19−23] Most studies leverage quantum-grade single-crystal bulk diamond with an NV-implanted thin layer requiring precision manufacturing.[24−26] Implementing the technology for integrated electronics is even more challenging, due to difficulties in adhering diamond to thin film devices or fabricating directly on diamond.[23,27,28] Alternative architectures of NV nanodiamond probes have been utilized for serial scanning or single point recording by conjugating single NV nanocrystals with cantilever structures.[29−32] These methods provide spatiotemporal sensitivity comparable to mainstay microelectronic magnetic characterization techniques such as superconducting quantum interference devices (SQUIDs) microscopy[33,34] and magnetic force microscopy (MFM)[35,36] but lack the parallel optical readouts available to NV magnetometry. A subset of these new designs rely on hybridization with single NV diamond nanoparticles (NVNPs) that are primarily emerging as highly photostable fluorescent imaging probes,[37−39] which have also been utilized for direct magnetomechanical manipulation and detection of biomolecules.[17,40] NVNPs are synthesized by more simplified processes including milling of high-pressure/high-temperature fabricated diamonds, laser ablation, or detonation[26,41] exhibiting reduced purity, NV distribution uniformity issues, and limited coherence times, compared with industrially grown slabs.[26] Nonetheless, their intrinsic ability to be integrated with ODMR presents new opportunities in magnetic characterization, including visualization of magnetic fields generated by currents in conductive patterned devices. A small number of

Received: January 29, 2025
Revised: May 9, 2025
Accepted: May 13, 2025

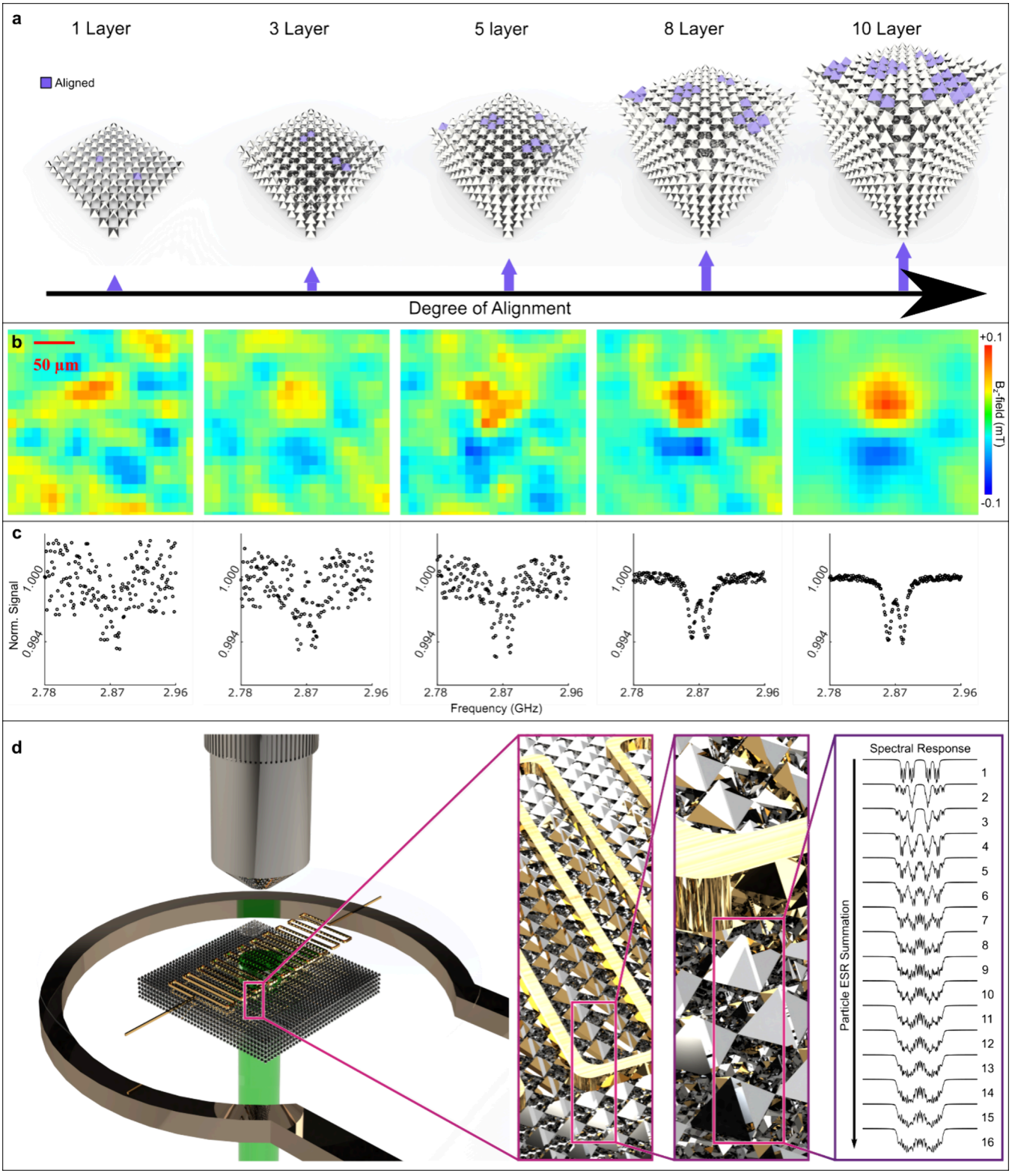

Figure 1. Increased alignment of multilayered nitrogen vacancy diamond nanoparticles (NVNP) relying on nucleation sites from previous layers to promote improved sensitivity to magnetic fields. (a) Depiction of aggregates of aligned particles with increasing coverage coinciding with increasing layer count. (b) Sensitive ODMR map of magnetic flux profile of a dipole emerging from the surface of a 100 μm × 100 μm, 30-nm-thick thin-film iron oxide probed by multiple layers of NVNPs (rightmost panel has 30 layers) and decreasing in sensitivity to a randomly aligned single NVNP layer (leftmost panel). Scale bar = 50 μm. (c) Increased layering corresponds to decreased MW spectral noise. (d) Schematic of magnetometry setup (not to scale) for measuring on-chip charge fluctuations using multilayered NVNPs. A 532 nm excitation pulse is applied to particles from below with fluorescence collected at 637 nm by the objective above sample, with MW (2.78−2.96 GHz) applied by a printed circuit antenna proximal to samples during current propagation. Right: estimated particle electron spin resonance (ESR) profiles of an example crystallographic orientation calculated over increasing levels of aggregation and alignment.

https://doi.org/10.1021/acs.nanolett.5c00656
Nano Lett. XXXX, XXX, XXX−XXX

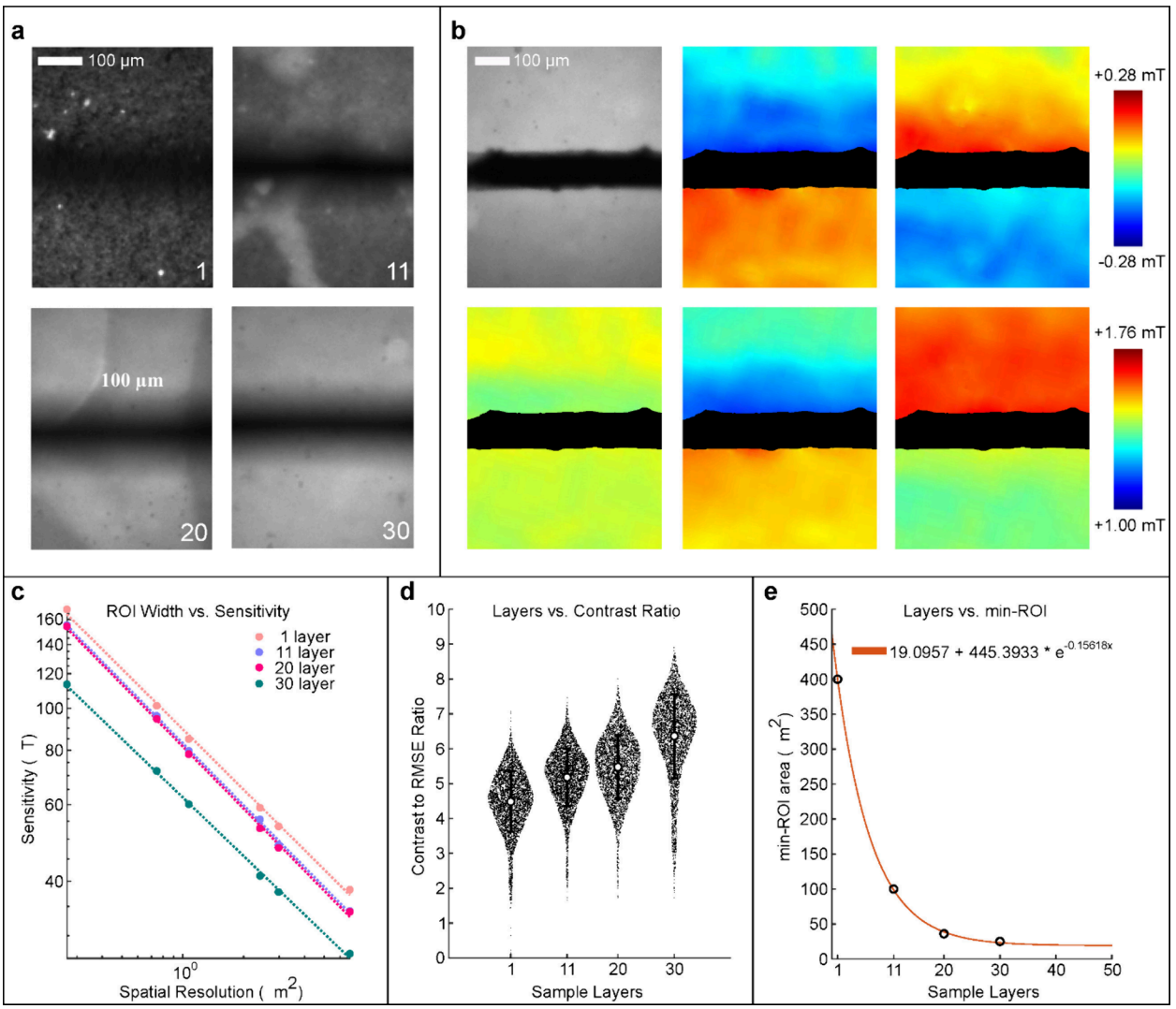

Figure 2. Improved sensitivity of NVNP samples with increasing layer strata. (a) (left to right) 1, 11, 20, and 30 layer samples under 8× magnification. (b) ODMR measurements of magnetic field in response to a DC current of 33 mA injected through a 100-μm-diameter wire. (Top left) raw image of wire and 30-layer sample; (bottom left) measurement of magnetic field magnitude with 0 mA current. (Bottom middle and bottom right) measurement of field magnitude with 33 mA current applied in opposing polarity. (Top middle and top right) subtraction of applied current and zero current measurements to reveal a B_z field. (c) Sensitivity, defined as the minimum detectable magnetic field, and its dependence on spatial resolution. Trends show a linear relationship for all layer counts. Performance, defined as the reciprocal slope offset, increases with increased layer count. (d) Ratio of spectral contrast to the RMSE of the best-fit curve to data as compared with layer count. (e) Comparison of layer count vs minimum ROI area.

studies utilized aggregates of NVNPs for surface-wide magnetometry[42,43] but spin orientations in aggregate NVNPs are inherently misaligned, precluding the use of such preparations for coherent determination of magnetic field vectors normally achieved by monocrystalline diamonds. A post-processing method for layering NVNPs with aligned NV center orientations can potentially facilitate superior NV magnetometry by allowing sensitive detection combined with simplified probe preparation. In this study, we present a novel and reproducible protocol for creating densely stacked monolayers of NVNPs with inherent interlayer alignment for sensitive measurement of local magnetic field perturbations induced by microelectronic currents. We establish spatial characteristics of deposited aggregates and demonstrate their ability to capture magnetic dipoles from conducting microwires via ODMR. We then generate NVNP-mediated visualization maps of currents generated by microfabricated 100 nm Ti/Au traces with single-micrometer spatial resolution. Using electron microscopy analysis and computational methods, we explain the mechanism of detection by predicting a level of up to 20% alignment across multiple tiers of the multilayer NVNP preparation required to achieve sensitivities measured experimentally. Our approach forms a novel accessible protocol that can be used for broad applications in micromagnetometry.

INCREMENTAL LAYERING OF NVNPs INCREASES PERFORMANCE

Interparticle interactions within solution milieu during solvent evaporation govern bottom-up nanoparticle self-assembly into highly tunable ordered superlattices, generating unique structural alignment and functionality.[44] Self-aligned superlattice diamond-NV sensors fabricated by polydimethylglutarimide (PMGI) wet etching of nanopatterned pillars,[45] microwave (MW) plasma chemical vapor deposition (CVD)

https://doi.org/10.1021/acs.nanolett.5c00656
Nano Lett. XXXX, XXX, XXX−XXX

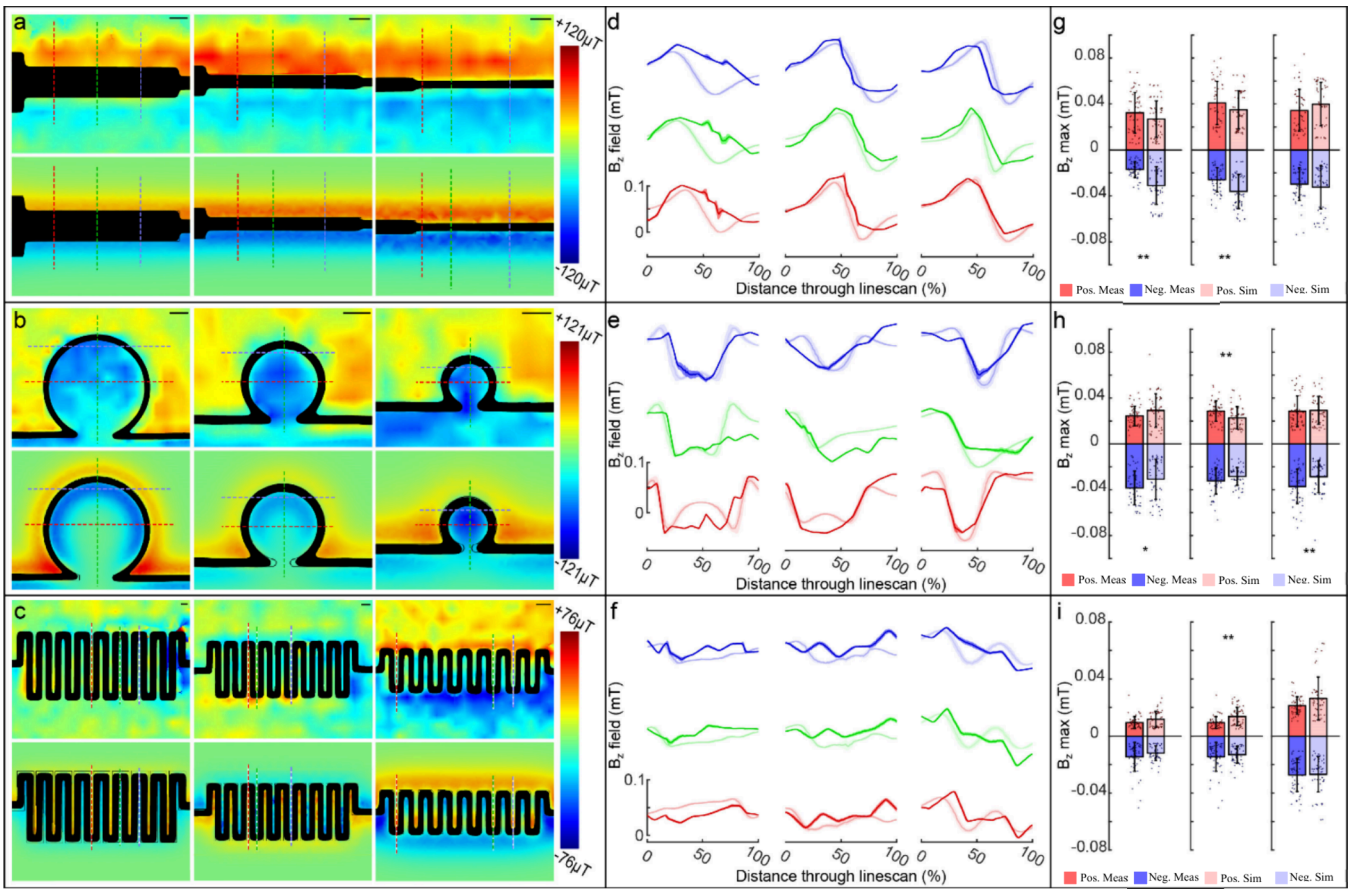

Figure 3. Direct ODMR measurements and corresponding finite element quantifications of magnetic field amplitude and distribution in variable microscale geometries. (a−c) B_z-field maps of patterns in response to DC current. Top panels show measured B_z field while bottom panels show the B_z field predicted by finite-element modeling. All scale bars represent 20 μm. (d−f) Corresponding plots for B_z field across longitudinal lines from widefield ODMR maps highlighted in panels (a)−(c). Shaded region denotes ± one standard deviation from the mean; dark bars represent ODMR measurements while lighter bars represent simulations. (g−i) Comparison of maxima and minima between measured (darker shading) and simulated (lighter shading) positive and magnetic field dipole components. Error bars represent ± one standard deviation from the mean. [Legend: (*) $p < 0.05$, (**) $p < 0.01$).]

of umbrella-shaped patterned protrusions,[46] or functionalization through amine-reactive cross-linking[47] show vast improvements in sensor sensitivity but require highly involved nanolithography. Other powerful examples include spin-wave electronic sensors probed using ODMR by exploiting randomly scattered nanodiamonds on patterned substrates,[48] and single nanodiamonds levitated in vacuum to greatly improve sensitivity and readout resolution.[49] But these efforts also require specialized techniques that are not trivial to implement at scale. We theorize that increased particle clusters built on spontaneously self-assembled "nucleation sites" expanding with increasing layer count can promote ordered clustering to improve readout quality and sensitivity, having been previously observed in ZnO,[50,51] ZnO/TiO_2,[52] and CuO nanostructures.[53] Figure 1a depicts increasingly aligned interlattice particle aggregates growing in size and quantity and coinciding with higher layer count. More numerous and larger aligned aggregates will inherently enable more coherent reconstruction of magnetic flux profiles for a dipole emerging at the sample surface compared with randomly aligned NVNPs. This is exemplified by the magnetic flux profile of a dipole emerging from the surface of a 100 μm × 100 μm, 30-nm-thick thin film of iron oxide measured on 30 layers of NVNPs (Figure 1b). Figure 1c provides the corresponding MW spectra of this measured dipole, quantified at 121.5 nT absolute amplitude, and +68.6 and −52.9 nT positive and negative amplitudes, respectively (Figure 1b, rightmost panel), and equivalent to a 19.6 MHz difference between spectral dips (Figure 1c, rightmost panel). We estimate a spectral signal-to-noise ratio of 0.86 for a randomly aligned NVNP layer (Figure 1c, leftmost panel) and 11.89 for 25% NV centers aligned (Figure 1c, rightmost panel). These measurements demonstrate detectability of dipoles arising from nanoscale thin films using layered NVNPs and suggest the feasibility of using this architecture for measuring charge movement on similar substrates. To assess this capability, we used an experimental configuration (Figure 1d) consisting of standard ODMR setup consisting of a 532-nm laser source applied below the multilayer NVNP sample with fluorescence collected at the upright position and a range of microwave energy (2.78−2.96 GHz) applied by a printed circuit antenna surrounding the sample. Ensemble particle measurements create characteristic electron spin resonance (ESR) double peak (rightmost panel) from which magnetic field magnitude at a given pixel is calculated with increased fidelity for a higher layer count. We turned to leverage this approach for detecting magnetic dipoles of moving charges in microscale conducting elements without requiring specialized fabrication methodologies or materials.

https://doi.org/10.1021/acs.nanolett.5c00656
Nano Lett. XXXX, XXX, XXX−XXX

Layering NVNPs at increased layer counts (1, 11, 20 and 30) revealed higher sensitivity and spatial resolution for detecting magnetic dipoles arising from currents applied through a tungsten microwire (~100 μm in diameter) (Figure 2). Transmitted light images of layered NVNPs show a general upward signal trend corresponding to higher uniformity of the samples over the magnetometer FOV (Figure 2a, standard deviation was 0.284, 0.262, 0.252, and 0.196 for 1, 11, 20, and 30 layers, respectively). We achieved maximal surface hydrophobicity during manufacturing by applying an isopropyl alcohol wash to the NVNP sample, left to dry in ambient temperature between each layer deposition. Similar demonstrations show surface-particle and particle−particle hydrophobic interactions competing with electrostatic attraction to participate in highly uniform nanoparticle self-assembly.[44,54] We next evaluated the ability of this system to detect current-induced magnetic dipoles by applying a 33 mA direct current (DC) with either positive or negative polarity (Figure 2b). We observed a clear dipole reversal during change of current polarity (Figure 2b, top middle and right panels). Increased layer counts coincided with increased spatial resolution and sensitivity (Figure 2c). For a pixel size of 1 μm^2, we found sensitivity (minimum detectable signal) of 89.52, 83.65, 81.51, and 62.64 μT for 1, 11, 20, and 30 layers, respectively. Spatial resolution-dependent sensitivity (Figure 2c) reveals similar trends, with a slight decrease for 11- and 20-layer samples compared with single layer sample and a significantly higher performance for 30-layer samples. We find a contrast to RMSE ratio of 4.4856 ± 0.8674, 5.1793 ± 0.8208, 5.4780 ± 0.9084, and 6.3654 ± 1.2027 ($\mu \pm \sigma$) for 1, 11, 20, and 30 layers, respectively, supporting this observation (Figure 2d). Layering shows a plateau in spatial resolution during imaging of current with a predicted asymptote of 19.096 μm^2 (Figure 2e). This coincides with plateaus observed in irradiated NV bulk crystals with NV layer of several micrometers.[24−26]

MAGNETIC DIPOLE MEASUREMENTS IN MICROPATTERNED TRACES

We turned to testing the ability of layered NVNPs to detect magnetic fields generated by currents in microfabricated devices of various geometries and verified their agreement with finite element predictions (Figure 3). Two-dimensional (2D) ODMR maps were generated during current injection (25−33 mA) in three families of micropatterns: (1) fiducial lines of 64, 32, and 16 μm lateral diameter (Figure 3a, top left, top middle, and top right panel, respectively); (2) single turn inductors with 60, 30, and 15 μm radius (Figure 3b, top left, top middle, and top right panel, respectively); and (3) nine-turn meander inductors with overall length of 150, 120, and 100 μm (Figure 3c, top left, top middle, and top right panel, respectively). For every family, corresponding finite element predictions of magnetic field distribution were performed (Figures 3a−c, bottom panels corresponding to ODMR data in the top panels). Analysis of longitudinal line scans at multiple locations through the devices verify the emergence of magnetic dipole during current injection, with spatial characteristics correlating relatively well with modeling (Figures 3d−f), with Pearson product-moment coefficients between ODMR measurements and finite element models given in Table 1. We observed a predictable reduction in correlation for larger patterns in all families (for example, 0.46023 at 50 μm vs 0.88008 at 10 μm for fiducial lines, 0.68585 at 200 μm vs 0.94085 at 50 μm for single-loop inductors, and 0.18095 at 200 μm vs 0.71371 at 90 μm for meander inductors; see the leftmost subpanels in Figures 3d−f, respectively). This could be attributed to larger overall area of Ti/Au traces intruding the collection of NVNP fluorescence within the field of view (FOV). Comparison between the amplitudes of the measured and predicted magnetic dipole for variable geometries (Figures 3g−i) reveals a positive magnetic dipole component (MDC) ranging between +30 and +40 μT (predicted: +25 to +40 μT) and a negative magnetic dipole component ranging between −15 and −30 μT (predicted: −30 to −35 μT) for fiducial lines (Figure 3g). Similar quantifications reveal positive MDC of +25 to +30 μT (predicted: +20 to +30 μT) and negative MDC of −30 to −37 μT (predicted: −27 to −32 μT) for single turn inductors (Figure 3h), and +10 to +20 μT (predicted: +10 to +25 μT) and −15 to −25 μT (predicted: −10 to −25 μT) for meandering inductor geometries (Figure 3i). Amplitudes were found to be similar ($p < 0.01$) for all small-feature geometries (rightmost panels). This demonstrates the ability of layered NVNPs to detect magnetic field amplitude from micropatterned traces with microscale spatial resolution.

Table 1. Pearson Product-Moment Coefficients for Comparing between ODMR Measurements and Finite-Element Models

	Pearson Product-Moment Coefficient[a]		
device	Scan 1 (Blue)	Scan 2 (Green)	Scan 3 (Red)
50 μm Fiducial	0.46023 *	0.56629 *	0.66336 *
20 μm Fiducial	0.95656 **	0.94843 **	0.90451 **
10 μm Fiducial	0.88008 **	0.83348 **	0.99412 **
200 μm Single Loop	0.91269 **	0.73826 **	0.68585 *
100 μm Single Loop	0.59843 *	0.79149 **	0.92338 **
50 μm Single Loop	0.91103 **	0.92212 **	0.94085 **
300 μm Inductor	0.46655 *	0.42215 *	0.43593 *
200 μm Inductor	0.18095	0.24422	0.31237 *
90 μm Inductor	0.71371 **	0.79462 **	0.75962 **

[a]Legend: (*) $p < 0.05$, (**) $p < 0.01$).

LAYERING IS CORRELATED WITH INTERCLUSTER PARTICLE ALIGNMENT

To arrive at a possible mechanistic relationship between magnetic field measurement quality and NVNP layering, we performed an analysis of scanning electron microscopy (SEM) images at different layer counts and related them to predicted interparticle alignment that could account for increased performance (Figure 4). Classifying particles by structural alignment defined as their relative angle of axis revealed an increase in the number of aggregates with preferential directionality of particles as the number of layers increased (Figures 4a and 4b). Particles that fell into clusters of similar orientations were identified with the same-color overlay (Figure 4a). To quantify how layering impacted these clusters, the mean cluster quality (MCQ) was calculated for each layer count, showing an increase in MCQ with increased layer count (Figure 4b). Multilayer samples all showed a marked increase in MCQ compared with a single layer sample but an insignificant increase between 11 and 20 layer samples, corresponding to trend seen in sensitivity measurements for these same layer counts (Figure 2c). Based on these aggregation levels, Monte Carlo MW spectra simulations of NVNP samples were generated to determine whether the physical preferential orientation of the particles can correspond

https://doi.org/10.1021/acs.nanolett.5c00656
Nano Lett. XXXX, XXX, XXX−XXX

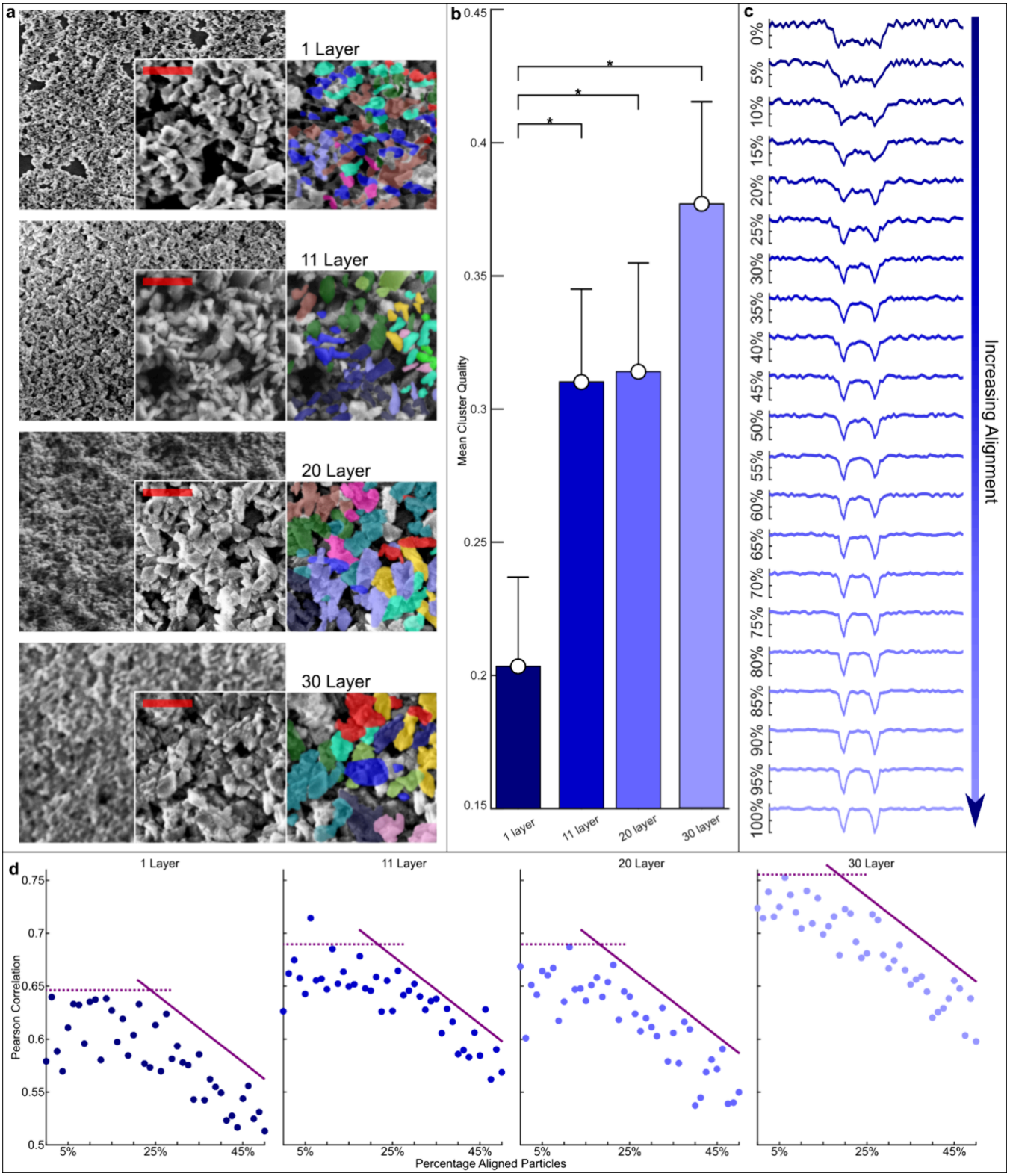

Figure 4. Scanning electron microscopy (SEM) analysis of multilayered NVNPs reveals structural directionality correlating with sensitivity of magnetic field measurements. (a) Example SEM images of layered particles; regions of interests (ROIs) with dimensions of 1.5 μm × 1.5 μm (insets) were analyzed by segregating single particles and determining their relative angle of axis (right: colored overlay of example ROIs). Scale bar = 0.5 μm. (b) Number of layers vs mean cluster quality (MCQ) as a measure of the mean number of same cluster neighbors a given particle exhibited for each cluster. Error bars represent standard deviation. (c) Monte Carlo simulation of spectral response for different layer counts and for a range of 0% to 100% lattice NVNP alignment. (d) Pearson correlation of measured spectral data to simulation data in panel (c) for a range of 0 to 50% alignment. Dual estimated asymptotes are shown for each condition (dashed and solid purple).

https://doi.org/10.1021/acs.nanolett.5c00656
Nano Lett. XXXX, XXX, XXX−XXX

with the alignment of the NV centers within the diamond lattice (Figure 4c). Simulated MW spectral responses were generated with a range of 0% to 100% lattice alignment of particles. Pearson correlation of measured spectral data to these simulations revealed an increased correlation to aligned simulations with increased layering, with 11- and 20-layer samples performing similarly (see Figures 4d and 2c−e). This analysis supports a mechanism whereby increased preferential lattice alignment correlates with increased layer count and could be a contributing factor in the increased sensitivity observed experimentally.

Here, we introduce a highly accessible micromagnetometry technique that utilizes self-aligned multilayered NVNPs to enable the detection of magnetic fields at microscale spatial resolution. We demonstrate the ability of the method to detect fields generated by currents in thin-film micropatterned electronic elements with implications for the development of new magnetic probes for measuring charge fluctuations in situ. Our electron microscopy analysis demonstrates structural alignment during aggregation. This could, in principle, account for NV center alignment and the improved ODMR sensitivities achieved here. We note that no additional preprocessing of NVNPs or specialized configurations were required for this performance. Previous studies indicate that electrostatic interactions at surface functionalized groups promote aggregation, resulting in energetically favorable configurations of extended bond lengths and enhanced stability at vacancy sites.[55] Alternative approaches to NVNP superstructure assembly have utilized techniques such as gradient force optical tweezers for highly precise real-time trapping and alignment at single particle resolution.[56] Other examples include octadecanethiol-based self-assembled monolayers,[57] specialized fiber optics,[42,43] and electrochemical cell systems[58] to achieve controlled organizations. Direct optical or electrochemical control provides superior accuracy of assembly. However, the methodology presented here offers a highly simplified mesoscopic-scale process, with no requirement for specialized instrumentation to guide superstructure formation at a larger scale. A specific and potentially impactful avenue of this technology is using layered NVNPs in biomedical applications for characterizing electromagnetic imaging and recording agents of biophysical events in excitable cells for neuroscience and cardiology.[23,59−61] By avoiding the requirement for fabricating devices directly on diamond or resorting to low-throughput serial scanning of the sample, our method offers an adoptable process for determining device performance and spatial distribution of magnetic field response to inform new and more powerful designs. Other promising efforts demonstrating high-throughput controlled deposition of NVNPs use high-density bubble printing by direct laser writing of NVNPs that preserve particle spin properties and allow for robust ODMR measurements.[62] Combining this approach and other precision patterning of NVNPs with incremental layering demonstrated here will provide a path to greatly improve applications of nanodiamonds for sensing and catalyze the advent of emerging materials such as magnetoelectric composites for quantum sensing, signal modulation and biological stimulation.[63−66] At present, our method is tested only with carbon-based nanodiamonds. However, further work may allow for its adaptation to assembly of superstructures of other spin defect nanoparticle types such as silicon carbide that can open the door to electromagnetic characterization of high-powered electronics and environmental sensors.[67]

METHODS

Micromagnetometry. A custom-made ODMR magnetometer was built utilizing a flexible PCB MW loop antenna (d = 1 mm, 50 Ω impedance matched) integrated with a 532-nm laser (Model OBIS 532−80 LS 1264453, Coherent, Santa Clara, CA) and wide-field microscope (Model SM-LUX HL, Leica Biosystems, Wetzlar, Germany). MW signals were generated using an RF signal generator (Model SG 384, Stanford Research Systems, Sunnyvale, CA) and fed through an RF amplifier (Mini-circuits ZHL-16W-43-S+, Scientific Components Corp., Brooklyn, NY) connected to the antenna. A bias magnetic field was generated using a Halbach array (k = 2) constructed using a neodymium block magnet (BCCC-N52, K&J Magnetics) placed below the layered NVNP sample. Bias field was measured to be 0.9 mT at the sample surface to sufficiently reduce strain and electric field effects and increase magnetic field sensitivity.[68] Fluorescence signal changes during current injection were captured using an upright microscope (Model SM-LUX HL, Leica Biosystems, Wetzlar, Germany) mounted with a CMOS camera (Model CS165MU1, Thorlabs, Inc., Newton, NJ) operating at 12 frames/s and a resolution of 720 × 540 pixels with a corresponding region of interest (ROI) size of 527 μm × 395 μm. A total of 181 frames surrounding the resonance at ∼2.87 GHz were acquired while sweeping between 2.78 and 2.96 GHz at 1 MHz intervals for a total of 181 data points per pixel and an acquisition time of 15 min. The image capture and delivery of microwaves and lasers were directly controlled through MATLAB (MathWorks, Inc. Natick, MA, USA) interface and in-house MATLAB routines.

Preparation of Layered NVNP Samples. To prepare layered NVNP samples, we delineated a 5 mm × 5 mm region at the center of microglass wafers (thickness = 160−190 μm) and applied the region with isopropyl alcohol (IPA) that was then left to evaporate to form a hydrophobic region. This step was repeated three times. We then applied 2 μL of 1 mg/mL fluorescent nanodiamonds (Catalog No. 798088, Sigma−Aldrich, St Louis, MO) onto the center of the hydrophobic region and allowed the solution to dry in room temperature (RT) for 2 h to allow NVNPs to settle. These steps were repeated to achieve the desired number of layers. For samples used in measuring field distributions at different microwire arrangements, we used 100-μm-diameter tungsten wire that was affixed to a 2 in. × 3 in. glass slide that was positioned face down onto the layered NVNP sample with the wire centered within the microscope field of view (FOV). For all samples, NVNPs were measured at average size of 130 nm using dynamic light scattering and profilometry was carried out on layered samples (Model DEP KLA-Tencor P7 profilometer (KLA Corporation, Milpitas, CA, USA). Optimal NVNP density to yield uniform monolayers was determined by initially testing a range of concentrations and selecting values that did not yield unwanted gaps or excess aggregation.

Device Microfabrication. Standard photolithography was used to fabricate three families of microdevices. The first contained a series of fiducial wires with stepwise decreases in trace width intended to isolate the effect of the geometry width on field detectability. The second was a series of single-turn coils with varying diameters to elucidate the magnetic field distribution around circular loops. The third is a series of meandering inductors with differing lengths and trace widths. These served as a method for evaluating the effect of tight turn-to-distance ratios on the magnetic field spread. Glass

https://doi.org/10.1021/acs.nanolett.5c00656
Nano Lett. XXXX, XXX, XXX−XXX

substrates were spin-coated with S183 photoresist (30 s, 3000 rpm, 1.3 μm thickness) baked at 110 °C for 1 min, followed by soft contact lithography (Karl Suss MA6, 15 s exposure time, 10 mW/cm^2 broadband mercury lamp) to pattern traces. Samples were developed in MF-321 (Kayaku Advanced Materials, Inc., Westborough, MA, USA) for 60 s, washed with deionized (DI) water, and dried with N_2. A Ti/Au bilayer (10/100 nm, respectively) was evaporated using e-beam deposition, and samples were then rinsed with IPA and DI water and dried with N_2 and lifted off in an ultrasonic bath at a medium−high vibration rate with acetone. This was followed by a 10-s oxygen plasma treatment of the descum surface (Model YES R3 Plasma Asher, 250 W, 80 SCCM O_2).

Finite Element Simulations. Magnetic-field profiles were simulated by using COMSOL Multiphysics 5.5 (COMSOL, Inc., Stockholm, Sweden). Computer-aided designs representing respective microfabricated geometries were imported into COMSOL and the electric currents (ec) and magnetic field (mf) interfaces of the AC/DC Module. Input current was applied between two ports at opposite edges of the simulation arena, and resulting magnetic field profiles were quantified at planes 50 μm above the device surface as the z-component of magnetic flux density (B-field) reflecting ODMR readouts. Field maps obtained were exported to MATLAB (MathWorks, Inc., Natick, MA) for further processing and analysis. Maximum and minimum magnetic field from each empirical dataset was compared to its respective simulation dataset.

Scanning Electron Microscopy Analysis. Scanning electron microscopy (SEM) analysis was performed on NVNP samples prepared on Si/SiO_2 wafers by using the same methods for ODMR measurements. Sets of images were taken of 1, 11, 20, and 30 layers and imported to the Fiji open source image processing software[69] for analysis. Each particle was outlined, and a set of random ROIs was generated for each layer count with the orientation (directionality) of each particle determined by the angle of its long axis. Clusters were then defined by assigning a particle to a cluster if and only if its angle was within the tolerance level defined as the mean orientation of the cluster and less than 2.3 μm from another particle that was already part of that cluster. Cluster quality (CQ) was calculated to determine the closeness of particles within a cluster with the mean number of same cluster neighbors, with mean cluster quality (MCQ), defined as

$$\mathrm{MCQ} = \mu_{\mathrm{unique}}\left(\bigcup_{0}^{n} d_{\mathrm{particle},n} < d_{\mathrm{particle,max}}\right) \quad (1)$$

where d is the interparticle distance and μ is a binary coefficient representing a unique particle pair.

Computational Modeling of Optical Responses. A simulation of the optical response from NV centers was performed using in-house MATLAB routines to further study observations within SEM analysis. Particles were assumed to have an equal proportion of NVs in all four crystallographic orientations, and the average size was measured at 130 nm using dynamic light scattering. Magnetic field was defined, and a corresponding reference NV axis vector system was created within MATLAB to represent a tetrahedral geometry with a user-defined number of orientations within the field of view. Random orientations for NV geometries were generated by utilizing a three-dimensional rotation matrix. For each orientation, the yaw, pitch, and roll for the rotation matrix were randomly drawn from a uniform distribution with support (0,1). Random trials were reproducible by setting the MATLABs random number generator seed to 1. Each reference NV vector was then multiplied by the rotation matrix to create a new random NV orientation. The component of the arbitrary magnetic field was determined along each NV axis for a given orientation, and the fluorescence response was calculated. Individual responses were then summed to calculate the overall simulated response from the multiple particles. To evaluate the effect of particle lattice alignment, an alignment factor was defined as the fraction of particle lattices aligned with one another and tested for 0−100% alignment in steps of 5%. Measured spectral data was correlated with simulation data for ranges of 0−50% in steps of 5% (Pearson correlation).

AUTHOR INFORMATION

Corresponding Author

Aviad Hai − *Department of Biomedical Engineering and Department of Electrical and Computer Engineering, University of Wisconsin−Madison, Madison, Wisconsin 53706, United States; Wisconsin Institute for Translational Neuroengineering, University of Wisconsin−Madison, Madison, Wisconsin 53792, United States;* orcid.org/0000-0002-4556-3048; Phone: 608-890-3411; Email: ahai@wisc.edu

Authors

Yash Gokhale − *Department of Biomedical Engineering, University of Wisconsin−Madison, Madison, Wisconsin 53706, United States; Wisconsin Institute for Translational Neuroengineering, University of Wisconsin−Madison, Madison, Wisconsin 53792, United States*

Brandon S. Coventry − *Wisconsin Institute for Translational Neuroengineering and Department of Neurological Surgery, University of Wisconsin−Madison, Madison, Wisconsin 53792, United States;* orcid.org/0000-0001-5524-0261

Tsani Rogers − *Department of Biomedical Engineering, University of Wisconsin−Madison, Madison, Wisconsin 53706, United States*

Maya Lines − *Department of Neuroscience, Lawrence University, Appleton, Wisconsin 54911, United States*

Anna Vena − *Department of Biomedical Engineering, University of Wisconsin−Madison, Madison, Wisconsin 53706, United States*

Jack Phillips − *Department of Biomedical Engineering, University of Wisconsin−Madison, Madison, Wisconsin 53706, United States*

Tianxiang Zhu − *Department of Biomedical Engineering, University of Wisconsin−Madison, Madison, Wisconsin 53706, United States*

Ilhan Bok − *Department of Biomedical Engineering, University of Wisconsin−Madison, Madison, Wisconsin 53706, United States; Wisconsin Institute for Translational Neuroengineering, University of Wisconsin−Madison, Madison, Wisconsin 53792, United States;* orcid.org/0000-0002-4481-7843

Dariana Troche − *Department of Mechanical Engineering, University of Puerto Rico at Mayagüez, Mayagüez 00680, Puerto Rico*

Mitchell Glodowski − *Department of Biomedical Engineering, University of Wisconsin−Madison, Madison, Wisconsin 53706, United States*

https://doi.org/10.1021/acs.nanolett.5c00656
Nano Lett. XXXX, XXX, XXX−XXX

Adam Vareberg − *Department of Biomedical Engineering, University of Wisconsin−Madison, Madison, Wisconsin 53706, United States*
Suyash Bhatt − *Department of Electrical and Computer Engineering, University of Wisconsin−Madison, Madison, Wisconsin 53706, United States*
Alireza Ousati Ashtiani − *Department of Biomedical Engineering, University of Wisconsin−Madison, Madison, Wisconsin 53706, United States*
Kevin W. Eliceiri − *Department of Biomedical Engineering, University of Wisconsin−Madison, Madison, Wisconsin 53706, United States; Department of Medical Physics, University of Wisconsin−Madison, Madison, Wisconsin 53792, United States; Morgridge Institute for Research, Madison, Wisconsin 53715, United States*

Complete contact information is available at: https://pubs.acs.org/10.1021/acs.nanolett.5c00656

Author Contributions

[▽]Authors Y. Gokhale and B. S. Coventry contributed equally to this work.

Notes

The authors declare no competing financial interest.

■ ACKNOWLEDGMENTS

This work was supported by the National Institute of Neurological Disorders and Stroke and the Office of the Director's Common Fund at the National Institutes of Health (Grant No. DP2NS122605 to A.H.) and the National Institute of Biomedical Imaging and Bioengineering (Grant No. K01EB027184 to A.H.). This material is also based on research supported by the U.S. Office of Naval Research, under Award Nos. N00014-23−1-2006, N00014-22−1-2371, and N00014-25-1-2000 to A.H,. through Dr. Timothy Bentley and the Wisconsin Alumni Research Foundation (WARF). The authors gratefully acknowledge the use of facilities and instrumentation supported by NSF through the University of Wisconsin Materials Research Science and Engineering Center (No. DMR-1720415). We thank Dr. Mikhail Shapiro, Dr. Hunter Davis, Dr. Ron Walsworth, Dr. Matthew Turner and Dr. Shlomo Kolkowitz for advice on ODMR and for supplying printed circuit board RF antenna.

■ REFERENCES

(1) Taylor, J. M.; et al. High-sensitivity diamond magnetometer with nanoscale resolution. *Nat. Phys.* **2008**, *4*, 810−816.
(2) Maze, J. R.; et al. Nanoscale magnetic sensing with an individual electronic spin in diamond. *Nature* **2008**, *455*, 644−647.
(3) Maletinsky, P.; et al. A robust scanning diamond sensor for nanoscale imaging with single nitrogen-vacancy centres. *Nat. Nanotechnol.* **2012**, *7*, 320−324.
(4) Wolf, T.; et al. Subpicotesla Diamond Magnetometry. *Phys. Rev. X* **2015**, *5*, No. 041001.
(5) Barry, J. F.; et al. Sensitivity optimization for NV-diamond magnetometry. *Rev. Mod. Phys.* **2020**, *92*, No. 015004.
(6) Gruber, A.; et al. Scanning Confocal Optical Microscopy and Magnetic Resonance on Single Defect Centers. *Science* **1997**, *276*, 2012−2014.
(7) Zhukov, I. V.; Anishchik, S. V.; Molin, Yu. N. ODMR Spectroscopy of NV− Centers in Diamond Under High MW Power. *Appl. Magn. Reson.* **2017**, *48*, 1461−1469.
(8) Levine, E. V.; et al. Principles and techniques of the quantum diamond microscope. *Nanophotonics* **2019**, *8*, 1945−1973.
(9) Sotoma, S.; Terada, D.; Segawa, T. F.; Igarashi, R.; Harada, Y.; Shirakawa, M. Enrichment of ODMR-active nitrogen-vacancy centres in five-nanometre-sized detonation-synthesized nanodiamonds: Nanoprobes for temperature, angle and position. *Sci. Rep.* **2018**, *8*, 5463.
(10) Nizovtsev, A. P.; et al. A quantum computer based on NV centers in diamond: Optically detected nutations of single electron and nuclear spins. *Opt. Spectrosc.* **2005**, *99*, 233−244.
(11) Childress, L.; et al. Coherent Dynamics of Coupled Electron and Nuclear Spin Qubits in Diamond. *Science* **2006**, *314*, 281.
(12) Wrachtrup, J.; Jelezko, F. Processing quantum information in diamond. *J. Phys.: Condens. Matter* **2006**, *18*, S807−S824.
(13) Waldermann, F. C.; et al. Creating diamond color centers for quantum optical applications. *Diam. Relat. Mater.* **2007**, *16*, 1887−1895.
(14) Awschalom, D. D.; Hanson, R.; Wrachtrup, J.; Zhou, B. B. Quantum technologies with optically interfaced solid-state spins. *Nat. Photonics* **2018**, *12*, 516−527.
(15) Davis, H. C.; Ramesh, P.; Bhatnagar, A.; Lee-Gosselin, A.; Barry, J. F.; Glenn, D. R.; Walsworth, R. L.; Shapiro, M. G. Mapping the microscale origins of magnetic resonance image contrast with subcellular diamond magnetometry. *Nat. Commun.* **2018**, *9*, 131.
(16) Kuwahata, A.; Kitaizumi, T.; Saichi, K.; Sato, T.; Igarashi, R.; Ohshima, T.; Masuyama, Y.; Iwasaki, T.; Hatano, M.; Jelezko, F.; et al. Magnetometer with nitrogen-vacancy center in a bulk diamond for detecting magnetic nanoparticles in biomedical applications. *Sci. Rep.* **2020**, *10*, 2483.
(17) Toraille, L.; et al. Optical Magnetometry of Single Biocompatible Micromagnets for Quantitative Magnetogenetic and Magnetomechanical Assays. *Nano Lett.* **2018**, *18*, 7635−7641.
(18) Kitaizumi, T.; et al. Magnetic Field Generation System of the Magnetic Probe With Diamond Quantum Sensor and Ferromagnetic Materials for the Detection of Sentinel Lymph Nodes With Magnetic Nanoparticles. *IEEE Trans. Magn.* **2021**, *57*, 1−5.
(19) Wu, Y.; Jelezko, F.; Plenio, M. B.; Weil, T. Diamond Quantum Devices in Biology. *Angew. Chem., Int. Ed.* **2016**, *55*, 6586−6598.
(20) Hall, L. T.; Beart, G. C. G.; Thomas, E. A.; Simpson, D. A.; McGuinness, L. P.; Cole, J. H.; Manton, J. H.; Scholten, R. E.; Jelezko, F.; Wrachtrup, J.; Petrou, S.; Hollenberg, L. C. L. High spatial and temporal resolution wide-field imaging of neuron activity using quantum NV-diamond. *Sci. Rep.* **2012**, *2*, 401.
(21) Barry, J. F.; et al. Optical magnetic detection of single-neuron action potentials using quantum defects in diamond. *Proc. Natl. Acad. Sci. U. S. A.* **2016**, *113*, 14133−14138.
(22) Parashar, M.; Saha, K.; Bandyopadhyay, S. Axon hillock currents enable single-neuron-resolved 3D reconstruction using diamond nitrogen-vacancy magnetometry. *Commun. Phys.* **2020**, *3*, 1−13.
(23) Bok, I.; Vareberg, A.; Gokhale, Y.; Bhatt, S.; Masterson, E.; Phillips, J.; Zhu, T.; Ren, X.; Hai, A. Wireless agents for brain recording and stimulation modalities. *Bioelectron. Med.* **2023**, *9*, 20.
(24) Pham, L. M.; et al. Magnetic field imaging with nitrogen-vacancy ensembles. *New J. Phys.* **2011**, *13*, No. 045021.
(25) Hong, S.; et al. Nanoscale magnetometry with NV centers in diamond. *MRS Bull.* **2013**, *38*, 155−161.
(26) Achard, J.; Jacques, V.; Tallaire, A. Chemical vapour deposition diamond single crystals with nitrogen-vacancy centres: a review of material synthesis and technology for quantum sensing applications. *J. Phys. Appl. Phys.* **2020**, *53*, 313001.
(27) Nowodzinski, A.; et al. Nitrogen-Vacancy centers in diamond for current imaging at the redistributive layer level of Integrated Circuits. *Microelectron. Reliab.* **2015**, *55*, 1549−1553.
(28) Turner, M. J.; et al. Magnetic Field Fingerprinting of Integrated-Circuit Activity with a Quantum Diamond Microscope. *Phys. Rev. Appl.* **2020**, *14*, No. 014097.
(29) Balasubramanian, G.; et al. Nanoscale imaging magnetometry with diamond spins under ambient conditions. *Nature* **2008**, *455*, 648−651.

https://doi.org/10.1021/acs.nanolett.5c00656
Nano Lett. XXXX, XXX, XXX−XXX

(30) Kleinlein, J.; et al. NV-center diamond cantilevers: Extending the range of available fabrication methods. *Microelectron. Eng.* **2016**, *159*, 70−74.
(31) Appel, P.; Neu, E.; Ganzhorn, M.; Barfuss, A.; Batzer, M.; Gratz, M.; Tschope, A.; Maletinsky, P. Fabrication of all diamond scanning probes for nanoscale magnetometry. *Rev. Sci. Instrum.* **2016**, *87*, No. 063703.
(32) Ficek, M.; et al. Integration of Fluorescent, NV-Rich Nanodiamond Particles with AFM Cantilevers by Focused Ion Beam for Hybrid Optical and Micromechanical Devices. *Coatings* **2021**, *11*, 1332.
(33) Chatraphorn, S.; Fleet, E. F.; Wellstood, F. C.; Knauss, L. A.; Eiles, T. M. Scanning SQUID microscopy of integrated circuits. *Appl. Phys. Lett.* **2000**, *76*, 2304−2306.
(34) Fong, L. E.; Holzer, J. R.; McBride, K. K.; Lima, E. A.; Baudenbacher, F.; Radparvar, M. High-resolution room-temperature sample scanning superconducting quantum interference device microscope configurable for geological and biomagnetic applications. *Rev. Sci. Instrum.* **2005**, *76*, No. 053703.
(35) Yongsunthon, R.; Stanishevsky, A.; McCoy, J.; Williams, E. D. Observation of current crowding near fabricated voids in gold lines. *Appl. Phys. Lett.* **2001**, *78*, 2661−2663.
(36) Kazakova, O.; Puttock, R.; Barton, C.; Corte-Leon, H.; Jaafar, M.; Neu, V.; Asenjo, A. Frontiers of magnetic force microscopy. *J. Appl. Phys.* **2019**, *125*, No. 060901.
(37) Fu, C.-C.; et al. Characterization and application of single fluorescent nanodiamonds as cellular biomarkers. *Proc. Natl. Acad. Sci. U. S. A.* **2007**, *104*, 727−732.
(38) McGuinness, L. P.; et al. Quantum measurement and orientation tracking of fluorescent nanodiamonds inside living cells. *Nat. Nanotechnol.* **2011**, *6*, 358−363.
(39) Jones, Z. R.; Niemuth, N. J.; Robinson, M. E.; Shenderova, O. A.; Klaper, R. D.; Hamers, R. J. Selective imaging of diamond nanoparticles within complex matrices using magnetically induced fluorescence contrast. *Environ. Sci. Nano* **2020**, *7*, 525−534.
(40) Teeling-Smith, R. M.; et al. Electron Paramagnetic Resonance of a Single NV Nanodiamond Attached to an Individual Biomolecule. *Biophys. J.* **2016**, *110*, 2044−2052.
(41) Mochalin, V. N.; Shenderova, O.; Ho, D.; Gogotsi, Y. The properties and applications of nanodiamonds. *Nat. Nanotechnol.* **2012**, *7*, 11−23.
(42) Fedotov, I. V.; et al. Fiber-optic magnetometry with randomly oriented spins. *Opt. Lett.* **2014**, *39*, 6755−6758.
(43) Wojciechowski, A. M.; et al. Optical Magnetometry Based on Nanodiamonds with Nitrogen-Vacancy Color Centers. *Materials* **2019**, *12*, 2951.
(44) Boles, M. A.; Engel, M.; Talapin, D. V. Self-Assembly of Colloidal Nanocrystals: From Intricate Structures to Functional Materials. *Chem. Rev.* **2016**, *116*, 11220−11289.
(45) Wang, M.; Sun, H.; Ye, X.; Yu, P.; Liu, H.; Zhou, J.; Wang, P.; Shi, F.; Wang, Y.; Du, J. Self-aligned patterning technique for fabricating high-performance diamond sensor arrays with nanoscale precision. *Sci. Adv.* **2022**, *8*, eabn9573.
(46) Furuyama, S.; Tahara, K.; Iwasaki, T.; Shimizu, M.; Yaita, J.; Kondo, M.; Kodera, T.; Hatano, M. Improvement of fluorescence intensity of nitrogen vacancy centers in self-formed diamond microstructures. *Appl. Phys. Lett.* **2015**, *107*, 163102.
(47) Abendroth, J. M.; et al. Single-Nitrogen−Vacancy NMR of Amine-Functionalized Diamond Surfaces. *Nano Lett.* **2022**, *22*, 7294−7303.
(48) Koerner, C.; et al. Frequency multiplication by collective nanoscale spin-wave dynamics. *Science* **2022**, *375*, 1165−1169.
(49) Jin, Y.; Shen, K.; Ju, P.; Gao, X.; Zu, C.; Grine, A. J.; Li, T. Quantum control and Berry phase of electron spins in rotating levitated diamonds in high vacuum. *Nat. Commun.* **2024**, *15*, 5063.
(50) Gao, X. P.; et al. Rotor-like ZnO by epitaxial growth under hydrothermal conditions. *Chem. Commun.* **2004**, 1428.
(51) Sounart, T. L.; et al. Sequential Nucleation and Growth of Complex Nanostructured Films. *Adv. Funct. Mater.* **2006**, *16*, 335−344.
(52) Yang, H. G.; Zeng, H. C. Synthetic Architectures of TiO_2/$H_2Ti_5O_{11}{\cdot}H_2O$, $ZnO/H_2Ti_5O_{11}{\cdot}H_2O$, $ZnO/TiO_2/H_2Ti_5O_{11}{\cdot}H_2O$, and ZnO/TiO_2 Nanocomposites. *J. Am. Chem. Soc.* **2005**, *127*, 270−278.
(53) Teng, F.; et al. Synthesis of flower-like CuO nanostructures as a sensitive sensor for catalysis. *Sens. Actuators B Chem.* **2008**, *134*, 761−768.
(54) Choueiri, R. M.; Klinkova, A.; Thérien-Aubin, H.; Rubinstein, M.; Kumacheva, E. Structural transitions in nanoparticle assemblies governed by competing nanoscale forces. *J. Am. Chem. Soc.* **2013**, *135*, 10262−10265.
(55) Chang, L.-Y.; Osawa, E.; Barnard, A. S. Confirmation of the electrostatic self-assembly of nanodiamonds. *Nanoscale* **2011**, *3*, 958−962.
(56) Stewart, A.; Zhu, Y.; Liu, Y.; Simpson, D. A.; Reece, P. J. Optical Tweezers Assembled Nanodiamond Quantum Sensors. *Nano Lett.* **2024**, *24*, 12188−12195.
(57) Rao, S. G.; et al. Directed assembly of nanodiamond nitrogen-vacancy centers on a chemically modified patterned surface. *ACS Appl. Mater. Interfaces* **2014**, *6*, 12893−12900.
(58) Karaveli, S.; et al. Modulation of nitrogen vacancy charge state and fluorescence in nanodiamonds using electrochemical potential. *Proc. Natl. Acad. Sci. U. S. A.* **2016**, *113*, 3938−3943.
(59) Phillips, J.; et al. Enhanced magnetic transduction of neuronal activity by nanofabricated inductors quantified via finite element analysis. *J. Neural Eng.* **2022**, *19*, No. 046003.
(60) Bhatt, S.; et al. Wireless in vivo recording of cortical activity by an ion-sensitive field effect transistor. *Sens. Actuators B Chem.* **2023**, *382*, 133549.
(61) Hai, A.; Spanoudaki, V. C.; Bartelle, B. B.; Jasanoff, A. Wireless resonant circuits for the minimally invasive sensing of biophysical processes in magnetic resonance imaging. *Nat. Biomed. Eng.* **2019**, *3*, 69−78.
(62) Blankenship, B. W.; et al. Spatially Resolved Quantum Sensing with High-Density Bubble-Printed Nanodiamonds. *Nano Lett.* **2024**, *24*, 9711−9719.
(63) Singer, A.; Dutta, S.; Lewis, E.; Chen, Z.; Chen, J. C.; Verma, N.; Avants, B.; Feldman, A. K.; O'Malley, J.; Beierlein, M.; Kemere, C.; Robinson, J. T. Magnetoelectric Materials for Miniature, Wireless Neural Stimulation at Therapeutic Frequencies. *Neuron* **2020**, *107*, 631−643.e5.
(64) Kozielski, K. L.; Jahanshahi, A.; Gilbert, H. B.; Yu, Y.; Erin, O.; Francisco, D.; Alosaimi, F.; Temel, Y.; Sitti, M. Nonresonant powering of injectable nanoelectrodes enables wireless deep brain stimulation in freely moving mice. *Sci. Adv.* **2021**, *7*, eabc4189.
(65) Bok, I.; Haber, I.; Qu, X.; Hai, A. In silico assessment of electrophysiological neuronal recordings mediated by magnetoelectric nanoparticles. *Sci. Rep.* **2022**, *12*, 8386.
(66) Kim, Y. J.; et al. Magnetoelectric nanodiscs enable wireless transgene-free neuromodulation. *Nat. Nanotechnol.* **2025**, *20*, 121.
(67) de Vries, M. O.; Sato, S.-i.; Ohshima, T.; Gibson, B. C.; Bluet, J.-M.; Castelletto, S.; Johnson, B. C.; Reineck, P. Fluorescent Silicon Carbide Nanoparticles. *Adv. Opt. Mater.* **2021**, *9*, 2100311.
(68) Bok, I.; Ashtiani, A.; Gokhale, Y.; Phillips, J.; Zhu, T.; Hai, A. Nanofabricated high turn-density spiral coils for on-chip electro-magneto-optical conversion. *Microsyst. Nanoeng.* **2024**, *10*, 1−12.
(69) Schindelin, J.; et al. Fiji: an open-source platform for biological-image analysis. *Nat. Methods* **2012**, *9*, 676−682.

https://doi.org/10.1021/acs.nanolett.5c00656
Nano Lett. XXXX, XXX, XXX−XXX